


Minimal Kitaev-transmon qubit based on double quantum dots

D. Michel Pino¹, Rubén Seoane Souto¹, and Ramón Aguado^{1*}

Instituto de Ciencia de Materiales de Madrid (ICMM), Consejo Superior de Investigaciones Científicas (CSIC), Sor Juana Inés de la Cruz 3, 28049 Madrid, Spain

 (Received 4 October 2023; accepted 10 January 2024; published 1 February 2024)

Minimal Kitaev chains composed of two semiconducting quantum dots coupled via a superconductor have emerged as a promising platform to realize and study Majorana bound states (MBSs), which appear for fine-tuned configurations. We propose a hybrid qubit based on a Josephson junction between two such double quantum dots (DQDs) embedded in a superconducting qubit geometry. The qubit makes use of the 4π -Josephson effect in the Kitaev junction to create a subspace based on the even/odd fermionic parities of the two DQD arrays hosting MBSs. Deep in the transmon regime, we demonstrate that by performing circuit QED spectroscopy on such a hybrid Kitaev-transmon “Kitmon” qubit, one could observe distinct MBS features in perfect agreement with precise analytical predictions in terms of DQD parameters only. This agreement allows us to extract the Majorana polarization in the junction from the microwave response.

DOI: [10.1103/PhysRevB.109.075101](https://doi.org/10.1103/PhysRevB.109.075101)

I. INTRODUCTION

Majorana bound states (MBSs) appearing at the ends of one-dimensional topological superconductors [1–8] feature non-Abelian statistics that can be exploited for robust quantum information processing [9]. Although early experiments showed signatures consistent with their presence, other states mainly originating from disorder can mimic their behavior, making it hard to distinguish between trivial and topological states [10].

Artificial Kitaev chains circumvent the inherent disorder issues that commonly appear in other platforms. In their minimal version, two quantum dots (QDs) couple via a narrow superconductor that allows for crossed Andreev reflection (CAR) and single-electron elastic cotunneling (ECT) [11–17]. Minimal Kitaev chains can host localized MBSs when a so-called sweet spot is reached with equal CAR and ECT amplitudes. Although the states are not topologically protected, they share properties with their topological counterparts, including non-Abelian statistics [18,19]. Recent experiments have shown measurements consistent with predictions at the sweet spot regime [20], breaking a new ground for the investigation of MBSs and paving the way toward scaling a topologically protected long chain and Majorana qubits [6] with QDs.

Expanding on this idea, we propose here a qubit based on a minimal Kitaev Josephson junction with four QDs and embedded in a superconducting qubit geometry, Fig. 1. The Josephson potential of the QD array modifies the superconducting qubit Hamiltonian and splits the microwave (MW) transitions due to the (nearly) degenerate fermionic parities of the Kitaev chains. Deep in the transmon limit, the qubit frequency can be analytically written in terms of the energy

difference between both parities, which can be written in turn in terms of QD parameters, Eq. (12), in perfect agreement with full numerics (Fig. 4). This agreement allows us to extract the Majorana polarization (MP) of the QD chain, Eq. (10), a measure of the Majorana character of the ground-state wave function [14,21–23], from the MW response.

II. MODEL

The minimal realization of a DQD-based Kitaev chain can be written as

$$H_{\text{DQD}} = - \sum_i \mu_i c_i^\dagger c_i - t c_1^\dagger c_2 + \Delta c_1 c_2 + \text{H.c.}, \quad (1)$$

where c_i^\dagger (c_i) denote creation (annihilation) operators on the $i \in 1, 2$ quantum dot with a chemical potential μ_i , while t and Δ are the coupling strengths mediated by CAR and ECT processes across a middle superconducting segment, respectively [24]. In the many-body basis of occupation states $|n_1 n_2\rangle$, the eigenstates of the problem are bonding/antibonding combinations in each fermionic parity sector (odd $|\sigma^\pm\rangle \sim |10\rangle \pm |01\rangle$ and even $|e^\pm\rangle \sim |00\rangle \pm |11\rangle$) with eigenvalues $\epsilon_o^\pm = -\mu \pm \sqrt{t^2 + \delta^2}$ and $\epsilon_e^\pm = -\mu \pm \sqrt{\Delta^2 + \mu^2}$, where we have defined the average chemical potential $\mu = (\mu_1 + \mu_2)/2$ and the detuning $\delta = (\mu_1 - \mu_2)/2$. Using this language, single-particle excitations can be defined as transitions between the even and odd sectors. Importantly, MBSs correspond to zero-energy excitations between two ground states of different parity at the sweet spot $t = \Delta$ and $\mu = \delta = 0$ [11].

Using this idea, a minimal Kitaev Josephson junction can be written as $H_{\text{DQD}}^{\text{J}} = H_{\text{DQD}}^{\text{L}} + H_{\text{DQD}}^{\text{R}} + H_{\text{J}}$, where $H_{\text{DQD}}^{\text{L}}$ and $H_{\text{DQD}}^{\text{R}}$ are two left/right Kitaev chains based on Eq. (1), and the Josephson coupling reads

$$H_{\text{J}} = -t_{\text{J}} e^{i\phi/2} c_{\text{L},2}^\dagger c_{\text{R},1} + \text{H.c.}, \quad (2)$$

*ramon.aguado@csic.es

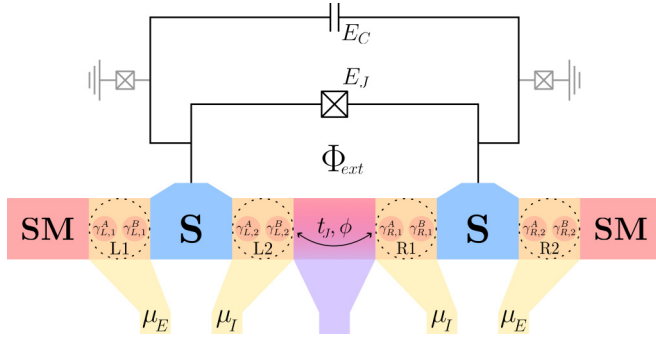


FIG. 1. Schematic illustration of the Kitaev-transmon device. A semiconductor (pink) can be gated (yellow) to create two minimal Kitaev chains (labeled as $\alpha = L, R$) comprising two quantum dots (labeled as $\beta = 1, 2$), connected via a middle superconductor (blue) and with chemical potentials μ_E and μ_I , external and internal, respectively. Each quantum dot contains two Majorana states $\gamma_{\alpha,\beta}^A$ and $\gamma_{\alpha,\beta}^B$. The two Kitaev chains are connected through a weak link (hopping t_J , purple region) forming a minimal Majorana Josephson junction. This minimal Kitaev junction is incorporated into a superconducting circuit, where the superconductors mediating the coupling between the QDs can act as transmon islands with a small charging energy E_C (tunable by extra junctions that can be opened to effectively ground either of the two islands, gray lines). The superconducting phase difference ϕ across the Kitaev junction is fixed by an external magnetic flux Φ_{ext} applied through a SQUID loop formed with a reference junction with Josephson energy E_J .

with $\phi = \phi_R - \phi_L$ being the superconducting phase difference and t_J the tunneling coupling between chains (see Fig. 1). The above model can be written in Bogoliubov–de Gennes (BdG) form as $H_{\text{BdG}}^{\text{JJ}} = \frac{1}{2} \Psi^\dagger H_{\text{DQD}}^{\text{JJ}} \Psi$, in terms of an eight-Majorana Nambu spinor

$$\Psi = (\gamma_{L,1}^A, \gamma_{L,1}^B, \gamma_{L,2}^A, \gamma_{L,2}^B, \gamma_{R,1}^A, \gamma_{R,1}^B, \gamma_{R,2}^A, \gamma_{R,2}^B)^T. \quad (3)$$

As we discuss below, the BdG model contains a standard Josephson coupling $\sim \cos \phi$ involving the “bulk” fermions together with a Majorana-mediated 4π Josephson effect of order $\sim \cos \frac{\phi}{2}$. The latter involves coherent single-electron tunneling with a characteristic energy scale E_M . From the perspective of circuit QED, previous papers have discussed how a Majorana junction in a transmon circuit splits spectral lines corresponding to different fermionic parities due to $E_M \neq 0$ [25–32]. In what follows, we discuss this physics in the context of the DQD minimal Kitaev Josephson junction to analyze the novel aspects that arise when this promising new platform is integrated into a superconducting circuit. Specifically, deviations from the sweet spot will be analyzed in terms of QD chemical potentials in the mirror-symmetric configurations, $\mu_{L,1} = \mu_{R,2} = \mu_E$ and $\mu_{L,2} = \mu_{R,1} = \mu_I$ (external versus internal), such that $\mu \equiv (\mu_E + \mu_I)/2$ and $\delta \equiv (\mu_E - \mu_I)/2$ (in what follows, we also consider $\Delta_L = \Delta_R = \Delta$ and $t_L = t_R = t$).

III. FOUR MAJORANAS SUBSPACE

A convenient way of gaining physical intuition is by projecting the above full model onto a low-energy subspace. The

simplest approach, widely used in previous literature [33–36], is to use a subspace spanned by just four MBSs: the two inner $\gamma_{L,2}^B$ and $\gamma_{R,1}^A$, and the two external $\gamma_{L,1}^A$ and $\gamma_{R,2}^B$. This results in an effective Josephson potential

$$V_{\text{DQD}}^{\text{JJ}}(\phi) = E_M \cos \frac{\phi}{2} \sigma_x + E_M^S \sin \frac{\phi}{2} \sigma_y + \lambda \sigma_z, \quad (4)$$

where σ_i are Pauli matrices defined onto the pseudospin parity space spanned by $|0\rangle \equiv |n_L = 0, n_R = 0\rangle$ and $|1\rangle \equiv |n_L = 1, n_R = 1\rangle$, where $n_L = n_{L,1} + n_{L,2}$ and $n_R = n_{R,1} + n_{R,2}$ are the fermion occupations in the left/right segments of the junction. E_M^S and λ are due to additional inter- and intra-Majorana couplings $\{\gamma_{L,1}^A \leftrightarrow \gamma_{R,1}^A, \gamma_{L,2}^B \leftrightarrow \gamma_{R,2}^B\}$ and $\{\gamma_{L,1}^A \leftrightarrow \gamma_{L,2}^B, \gamma_{R,1}^A \leftrightarrow \gamma_{R,2}^B\}$, respectively (for a detailed discussion, see Appendix A). In the mirror-symmetric case, $E_M^S = \lambda = 0$, which gives

$$V_{\text{DQD}}^{\text{JJ}}(\phi) = \frac{t_J}{2} \left[1 - \frac{\mu_E^2}{(t + \Delta)^2} \right] \cos \frac{\phi}{2} \sigma_x. \quad (5)$$

From this, it becomes clear that driving t_J would induce transitions between the qubit $|0\rangle$ and $|1\rangle$ states. Rotations along the equator can be achieved by coupling the Majorana states in the same Kitaev chain by detuning it away from the sweet spot, a term proportional to λ in Eq. (4).

While being able to capture some of the phenomenology, including the E_M renormalization with the external gates, this four-Majorana projection has important limitations. Most importantly, detuning the chemical potentials μ_E and μ_I away from zero affects the localization of the MBSs, which acquire some weight in “bulk” sites removed from the projection (for instance, a $\mu_E \neq 0$ induces weight of the order of $\sim \frac{\mu_E}{t}$ in the inner dots [11]). This makes the four-Majorana projection insufficient to describe the physics of the DQD junction [for a full derivation of Eq. (5) and a detailed discussion about the limitations of this projection, see Appendix A].

IV. BEYOND FOUR MAJORANAS

To go beyond the previous projection and its limitations, we choose the subspace spanned by the two lowest-energy many-body eigenstates $\{|o_L^-, o_R^-\rangle, |e_L^-, e_R^-\rangle\}$ resulting from diagonalizing each isolated segment in the basis of occupation states. The diagonal Hamiltonian in the bipartite Hilbert space $\mathcal{H}_L \otimes \mathcal{H}_R$ can be represented on the basis of joint eigenstates $\{|i_L, j_R\rangle = |i_L\rangle \otimes |j_R\rangle\}$ with $i, j = o^\pm, e^\pm$ (see Appendix B):

$$\tilde{H}_L + \tilde{H}_R = (P_L^{-1} H_L P_L) \otimes \mathbb{1}_R + \mathbb{1}_L \otimes (P_R^{-1} H_R P_R), \quad (6)$$

where P_α is the change-of-basis matrix onto the eigenbasis of each chain. The off-diagonal Josephson term \tilde{H}_J can be easily represented on the joint-occupation basis $\{|n_{L,1}, n_{L,2}\rangle \otimes |n_{R,1}, n_{R,2}\rangle\}_{n_{\alpha,i}=0,1}$ and then projected onto the eigenbasis by the change-of-basis matrix $P_L R = P_L \otimes P_R$, which allows us to obtain the Josephson potential analytically (see Appendix B). Specifically, for the mirror-symmetric case, the many-body eigenvalues $\epsilon_{e/o}^\pm$ are equal for both left and right chains, and this Josephson potential reduces to a very compact form

$$V_{\text{DQD}}^{\text{JJ}}(\phi) = \begin{pmatrix} 2\epsilon_o^- & E_M \cos \frac{\phi}{2} \\ E_M \cos \frac{\phi}{2} & 2\epsilon_e^- \end{pmatrix} \quad (7)$$

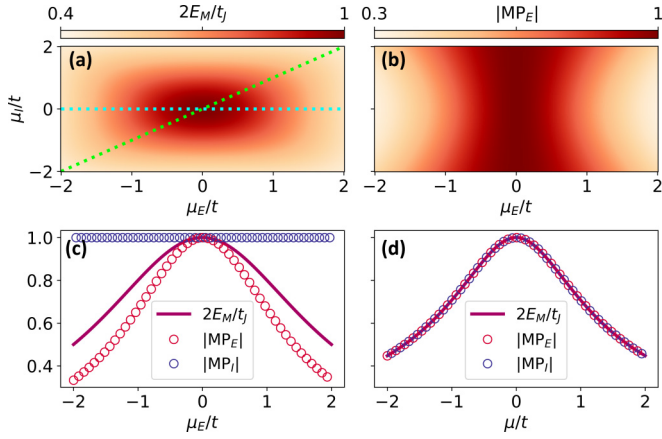


FIG. 2. Majorana polarization and Majorana coupling. (a) $2E_M/t_J$ and (b) $|MP_E|$ as a function of μ_E and μ_I . $2E_M/t_J$, $|MP_E|$, and $|MP_I|$ as a function of (c) μ_E with $\mu_I = 0$ and (d) $\mu_E = \mu_I = \mu$ [blue and green dotted lines in panel (a), respectively]. $\Delta/t = 1$ for all panels.

with

$$E_M = \frac{t_J \Delta t}{2(\mu + \epsilon_o^-)(\mu + \epsilon_e^-)} = \frac{t_J \Delta t}{2\sqrt{(t^2 + \delta^2)(\Delta^2 + \mu^2)}}. \quad (8)$$

Expanding Eq. (8) to leading order of μ and δ , we recover E_M in Eq. (5) for $t = \Delta$ and $\mu = \delta$ ($\mu_I = 0$).

V. MAJORANA POLARIZATION

For $t_J = 0$, the many body problem described above can be separated into two independent blocks of even ($\{|o_L^\pm, o_R^\pm\rangle, |e_L^\pm, e_R^\pm\rangle\}$) and odd ($\{|e_L^\pm, o_R^\pm\rangle, |o_L^\pm, e_R^\pm\rangle\}$) total parity, which

leads to a twofold-degenerate spectrum. To determine whether these degeneracies are associated with MBSs, we use the MP defined on the left Kitaev chain as $MP_i = \frac{w_i^2 - z_i^2}{w_i^2 + z_i^2}$, with $w_i = \langle o|c_i + c_i^\dagger|e\rangle$, $z_i = \langle o|c_i - c_i^\dagger|e\rangle$, and $i \in I, E$ (for convenience, we already use the mirror-symmetric notation). For the left DQD, we take $|e\rangle = |o_L^-, o_R^-\rangle$ and $|o\rangle = |e_L^-, o_R^-\rangle$, which gives

$$MP_{E/I} = \frac{t \Delta}{\pm \delta \mu - (\mu + \epsilon_o^-)(\mu + \epsilon_e^-)}, \quad (9)$$

where we have omitted the left subscript for simplicity. A similar treatment can be performed for the right chain where now the indexes I/E are exchanged.

For $t = \Delta$, $|MP_E|$ ($|MP_I|$) is maximum when $\mu = \delta$ ($\mu = -\delta$), that is, when $\mu_{L,2} = 0$ ($\mu_{L,1} = 0$), and it reads

$$MP_{I/E} = \frac{-E_M}{\frac{t}{2} \pm \frac{\delta \mu}{t} E_M} \quad (10)$$

with E_M given by Eq. (8). Note that for $\delta = 0$ or $\mu = 0$ ($\mu_E = \mu_I$ or $\mu_E = -\mu_I$, respectively), MP is equal on every QD and it is directly proportional to E_M , see Fig. 2. Therefore, a direct measurement of the MP via E_M is possible through MW spectroscopy, as we discuss now.

VI. HYBRID SUPERCONDUCTING QUBIT MODEL

We now study a DQD-based Majorana Josephson junction in a superconducting qubit geometry (namely a split junction shunted by a capacitor, with charging energy E_C [37]; see Fig. 1) described by the Hamiltonian

$$H = 4E_C(\hat{n} - n_g)^2 - E_J \cos(\hat{\phi}) + V_{\text{DQD}}^{\text{JJ}}(\hat{\phi} - \phi_{\text{ext}}). \quad (11)$$

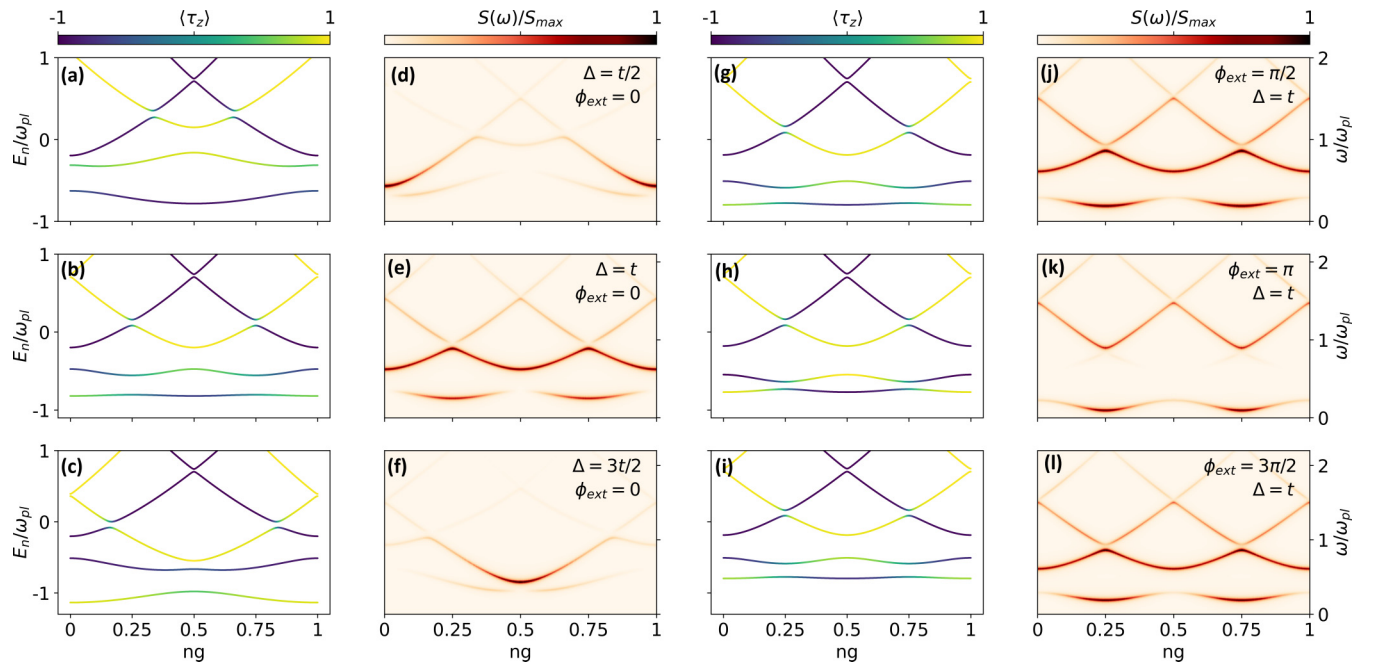


FIG. 3. MW spectroscopy in the charging regime. Levels, parity texture (τ_z), and $S(\omega)$ from the solutions of Eq. (11) against n_g with $\mu_E = \mu_I = 0$ for (a)–(f) $\Delta/t = 0.5, 1, 1.5$, and $\phi_{\text{ext}} = 0$; and (g)–(l) $\phi_{\text{ext}} = \pi/2, \pi, 3\pi/2$, and $\Delta = t$ (from top to bottom). $E_J = E_C = t$ and $t_J/t = 1$ in all panels. All energies are shown in units of the plasma frequency $\omega_{pl} = \sqrt{8E_J E_C}$.

Here, $\hat{n} = -i \frac{\partial}{\partial \phi}$ is the Cooper-pair number operator, conjugate to the junction superconducting phase difference $\hat{\phi}$, and $n_g = Q_g/(2e) = V_g/(2eC_g)$ is the gate-induced offset charge in the island (in units of Cooper pairs). The phase difference across the DQD Josephson junction can be controlled by the magnetic flux through the SQUID loop $\Phi_{\text{ext}} = \phi_{\text{ext}} \Phi_0/(2\pi)$, where $\Phi_0 = h/2e$ is the superconducting flux quantum. Using the solutions of (11) [38], the microwave (MW) absorption spectrum [39] of the superconducting island can be written in linear response as $S(\omega) = \sum_k |\langle k | \hat{n} | 0 \rangle|^2 \delta(\omega - \omega_{0k})$, where the index k orders the eigenstates of the system with increasing energies. This response measures the energy transitions $\omega_{0k} = \omega_k - \omega_0$ between the ground state $E_0 = \hbar\omega_0$ and the excited states $E_k = \hbar\omega_k$ and with a probability weighted by the matrix elements of \hat{n} .

Single-electron tunneling processes mediated by the off-diagonal terms of the DQD-based Josephson potential in Eq. (7) lead to very specific predictions in the spectrum that should be easily detected using standard circuit QED techniques. For example, crossing the sweet spot, while keeping $\mu_E = \mu_I = 0$, from the ECT-dominated regime [$t > \Delta$, Fig. 3(a)] to the CAR-dominated regime [$t < \Delta$, Fig. 3(c)], changes the fermionic parity of the GS. This is reflected as an *exact 1e shift in n_g in the MW spectra* [compare Figs. 3(d) and 3(f)]. At the sweet spot for $t = \Delta$, the intraband coupling leads to maximally mixed parity states $\langle \tau_z \rangle = 0$ with avoided crossings around $n_g = 0.25$ and 0.75 , Fig. 3(b). This results in an overall 1e-periodic MW spectrum with a strong low-frequency response near these gates, Fig. 3(e). Therefore, the intraband transition ω_{01} is a direct indication of an $E_M \neq 0$ in the spectrum.

VII. KITAEV-TRANSMON REGIME

A way to check that the low-frequency MW transitions ω_{01} near $n_g = 0.25$ and $n_g = 0.75$ are indeed due to parity mixing mediated by MBSs in the DQD junction, instead of quasiparticle poisoning [40–42], is to prove that they can be tuned by ϕ_{ext} , and reach a minimum value at $\phi_{\text{ext}} = \pi$, Figs. 3(j)–3(l). Note, however, that due to quantum phase fluctuations, the Josephson potential V_{DQD}^J in Eq. (11) depends on a phase drop that deviates from the external phase imposed by the circuit, hence resulting in a residual splitting at $n_g = 0.25$ that does not close completely at $\phi_{\text{ext}} = \pi$. This effect is shown in Fig. 4(a), where we plot the full ϕ_{ext} dependence corresponding to the MW spectra of Figs. 3(j)–3(l) at fixed $n_g = 0.25$. Interestingly, parity changes due to Majorana physics are already evident as a spectral hole near $\phi_{\text{ext}} = \pi$ in the transition ω_{02} . By tracing such a spectral hole in ω_{02} (or, equivalently, the appearance of the transition ω_{03}), we can identify when a true energy crossing occurs in the system as a function of increasing E_J/E_C ratios, Figs. 4(b) and 4(c). While, generally, an analytical expression of the energy splitting at $n_g = 0.25$ would require knowing the explicit form of the qubit wave functions, the deep transmon regime with $E_J/E_C \gg 1$ allows us to approximate these eigenfunctions to two coupled (parity-defined) harmonic-oscillator states sharpened around ϕ_{ext} . In this regime, the Kitmon qubit frequency $\omega_{\text{KIT}} \equiv \omega_{01}$ can be

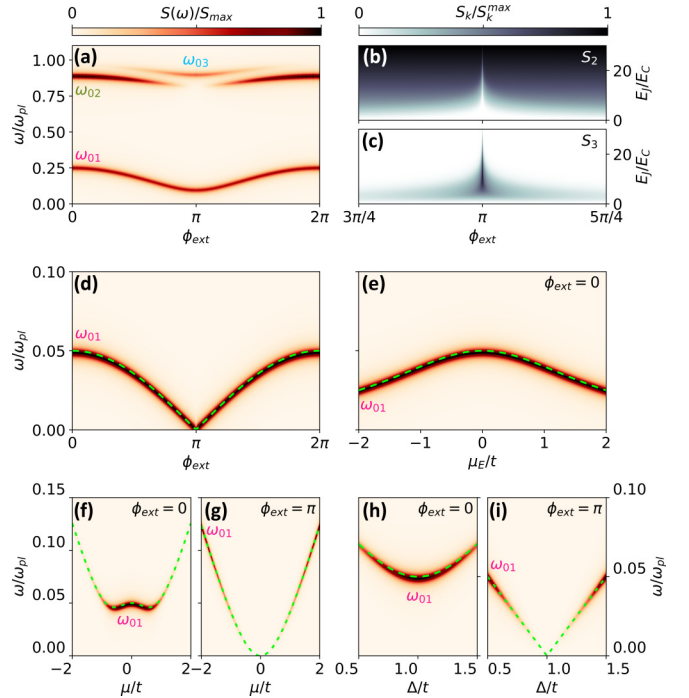


FIG. 4. Kitaev-transmon qubit spectroscopy. (a) Full phase dependence of the MW absorption spectrum of Figs. 3(g)–3(l) at $n_g = 0.25$. (b),(c) Spectral weights for transitions ω_{02} (S_2) and ω_{03} (S_3) as a function of ϕ_{ext} and E_J/E_C at the sweet spot ($\Delta = t$, $\mu_E = \mu_I = 0$). (d)–(i) MW absorption spectra as a function of (d) ϕ_{ext} at the sweet spot; (e) μ_E with $\mu_I = 0$ and $\Delta = t$ and $\phi_{\text{ext}} = 0$; (f),(g) $\mu_E = \mu_I = \mu$ with $\Delta = t$ and $\phi_{\text{ext}} = 0, \pi$; and (h)–(i) Δ/t with $\mu_E = \mu_I = 0$ and $\phi_{\text{ext}} = 0, \pi$. Green dashed lines correspond to the analytical qubit frequency ω_{KIT} in Eq. (12). For panels (d)–(i) we have fixed $E_J = 50E_C = 50t$, $t_J/t = 1$ for all panels. All energies are shown in units of the plasma frequency $\omega_{\text{pl}} = \sqrt{8E_J E_C}$.

written as

$$\omega_{\text{KIT}} \approx 2\sqrt{(\epsilon_e^- - \epsilon_o^-)^2 + E_M^2 \cos^2 \frac{\phi_{\text{ext}}}{2}} \quad (12)$$

[a detailed check of the validity of Eq. (12) for increasing values of E_J/E_C ratios can be found in Appendix D]. When $t = \Delta$ and $\delta = \pm\mu$ ($\mu_I = 0$ or $\mu_E = 0$), the qubit frequency is directly proportional to E_M ,

$$\omega_{\text{KIT}} \approx 2E_M \cos \frac{\phi_{\text{ext}}}{2} = \frac{t_J}{1 + (\mu/\Delta)^2} \cos \frac{\phi_{\text{ext}}}{2}. \quad (13)$$

A direct comparison between the full numerics and Eq. (12) against different parameters of the junction, Figs. 4(d)–4(i), demonstrates an almost perfect agreement. Therefore, MW measurements like the ones discussed here should allow us to check our predictions, e.g., the resonant behavior against μ_E in Eq. (13), see Fig. 4(e). More importantly, a measurement like the one shown in Figs. 4(f) and 4(g) (namely ω_{KIT} versus $\mu = \mu_E = \mu_I$, hence $\delta = 0$) would allow us to directly extract E_M and hence determine the MP polarization of the junction via Eq. (10).

In conclusion, we have proposed a minimal Kitaev-Transmon qubit based on a QD Josephson junction array

embedded in a superconducting circuit. Deep in the transmon regime with $E_J/E_C \gg 1$ we have found an analytical expression for the qubit frequency, Eq. (12), that allows us to obtain very precise predictions of its evolution against QD parameters, Fig. 4, and to extract the Majorana polarization. These predictions in terms of analytics would allow us to experimentally distinguish the physics discussed here from either quasiparticle poisoning or 4π phase slips due to QD resonances [43]. The Kitmon qubit architecture is a natural extension of the recent experimental implementations of nanowire-based double island devices [44], gatemons [45–48], and Andreev spin qubits [49], although free from the uncertainties originated from disorder. Most importantly, QD-based Josephson junctions embedded in a transmon circuit have recently been implemented experimentally [41,42,50]. In the strong Coulomb blockade regime, they have been used to show spin-split MW transition lines [51] forming a QD-based superconducting spin qubit coherently coupled to a transmon [52]. In this context, our DQD proposal could be seen as a minimal Majorana-based nonlocal parity pseudospin, Eqs. (7) and (12), coupled to a transmon. All this experimental progress, together with the recent demonstration of poisoning times of the order of milliseconds [53] and quasiparticle trapping engineering [54–57], make the physics discussed here within reach [58] with superconductor-semiconductor hybrid devices [59].

ACKNOWLEDGMENTS

We acknowledge financial support from the Horizon Europe Framework Program of the European Commission through the European Innovation Council Pathfinder Grant No. 101115315 (QuKIT), the Spanish Ministry of Science through Grants No. PID2021-125343NB-I00 and No. TED2021-130292B-C43 funded by MCIN/AEI/10.13039/501100011033, “ERDF A way of making Europe,” the Spanish Comunidad de Madrid (CM) “Talento Program” (Project No. 2022-T1/IND-24070), and European Union NextGenerationEU/PRTR. Support by the Consejo Superior de Investigaciones Científicas (CSIC) Interdisciplinary Thematic Platform (PTI+) on Quantum Technologies (PTI-QTEP+) is also acknowledged.

APPENDIX A: FOUR MAJORANAS SUBSPACE

1. Effective low-energy projection

To derive a quantitative low-energy description of our system, we project the full Hamiltonian $H_{\text{DQD}}^{\text{JJ}}$ —Eqs. (1) and (2) of the main text—onto the fermionic parity subspace that forms the superconducting qubit. This procedure considers both standard Josephson events due to Cooper pair tunneling, as well as anomalous Majorana-mediated events, where a single electron is transferred across the junction. Hence, we can distinguish two contributions of the Josephson potential, $V_J = V_J^{\text{bulk}} + V_{\text{DQD}}^{\text{JJ}}$. The first one takes into account the bulk contribution of the Bogoliubov–de Gennes (BdG) levels above the gap to the ground-state energy, which we just assume to be of the standard form $V_J^{\text{bulk}}(\phi) = -E_J \cos \phi$. The second contribution corresponds to the subgap sector, and it can be expressed as the projection onto a fermionic parity basis of an

effective model of four Majorana operators, $\gamma_{L,1}^A, \gamma_{L,2}^B \in L$ and $\gamma_{R,1}^A, \gamma_{R,2}^B \in R$, corresponding to the end modes of both chains. Its effective Hamiltonian takes the general BdG form

$$H_\gamma = \frac{i}{2} \begin{pmatrix} \gamma_{L,1}^A & \gamma_{L,2}^B & \gamma_{R,1}^A & \gamma_{R,2}^B \end{pmatrix} \times \begin{pmatrix} 0 & \lambda_{L1,L2} & \lambda_{L1,R1} & \lambda_{L1,R2} \\ -\lambda_{L1,L2} & 0 & \lambda_{L2,R1} & \lambda_{L2,R2} \\ -\lambda_{L1,R1} & -\lambda_{L2,R1} & 0 & \lambda_{R1,R2} \\ -\lambda_{L1,R2} & -\lambda_{L2,R2} & -\lambda_{R1,R2} & 0 \end{pmatrix} \begin{pmatrix} \gamma_{L,1}^A \\ \gamma_{L,2}^B \\ \gamma_{R,1}^A \\ \gamma_{R,2}^B \end{pmatrix}. \quad (\text{A1})$$

Our objective is now to relate $H_{\text{DQD}}^{\text{JJ}}$ to this general effective model of four Majoranas H_γ to obtain an explicit expression of its coefficients. Thus, we project the BdG form of the former, $H_{\text{BdG}}^{\text{JJ}}$ —Eqs. (1) and (2) of the main text using the Majorana spinor in Eq. (3) of the main text—onto the low-energy subspace of Majorana operators. To do that, we define a basis of fermionic operators

$$c_\alpha = \frac{1}{\sqrt{2}}(\gamma_{\alpha,1}^A + i\gamma_{\alpha,2}^B), \quad c_\alpha^\dagger = \frac{1}{\sqrt{2}}(\gamma_{\alpha,1}^A - i\gamma_{\alpha,2}^B), \quad (\text{A2})$$

and we compute the matrix elements of the resolvent of $H_{\text{BdG}}^{\text{JJ}}$,

$$G(\omega) = [(\omega + i\epsilon)\mathbb{I} - H_{\text{BdG}}^{\text{JJ}}]^{-1}, \quad \epsilon \rightarrow 0^+ \quad (\text{A3})$$

at $\omega = 0$ on the $\psi^0 = (c_L, c_R, c_L^\dagger, c_R^\dagger)_0^T$ state basis. The procedure is as follows: first of all, we calculate $G(\omega)$ by inverting the matrix $(\omega + i\epsilon)\mathbb{I} - H_{\text{BdG}}^{\text{JJ}}$ written on the Majorana state basis of the whole system,

$$\Psi = (\gamma_{L,1}^A, \gamma_{L,1}^B, \gamma_{L,2}^A, \gamma_{L,2}^B, \gamma_{R,1}^A, \gamma_{R,1}^B, \gamma_{R,2}^A, \gamma_{R,2}^B)_0^T. \quad (\text{A4})$$

Then, we evaluate this resolvent matrix at $\omega = 0$ and we project it onto the ψ^0 basis, expressed in terms of Ψ states as

$$\begin{aligned} (1 \ 0 \ 0 \ 0)_0^T &\equiv \frac{1}{\sqrt{2}}(1 \ 0 \ 0 \ i \ 0 \ 0 \ 0 \ 0)^T, \\ (0 \ 1 \ 0 \ 0)_0^T &\equiv \frac{1}{\sqrt{2}}(0 \ 0 \ 0 \ 0 \ 1 \ 0 \ 0 \ i)^T, \\ (0 \ 0 \ 1 \ 0)_0^T &\equiv \frac{1}{\sqrt{2}}(1 \ 0 \ 0 \ -i \ 0 \ 0 \ 0 \ 0)^T, \\ (0 \ 0 \ 0 \ 1)_0^T &\equiv \frac{1}{\sqrt{2}}(0 \ 0 \ 0 \ 0 \ 1 \ 0 \ 0 \ -i)^T. \end{aligned} \quad (\text{A5})$$

This gives rise to a 4×4 matrix

$$(\mathcal{H}_0^{-1})_{ij} = \langle \psi_i^0 | G(\omega = 0) | \psi_j^0 \rangle, \quad (\text{A6})$$

whose inverse

$$H_0 = \frac{1}{2} \sum_{i,j} \psi_i^{0\dagger} (\mathcal{H}_0)_{ij} \psi_j^0 \quad (\text{A7})$$

is the projection of $H_{\text{DQD}}^{\text{JJ}}$ onto the subspace of low-energy fermions. Finally, a simple change of basis $\psi^0 \rightarrow \psi^\gamma = (\gamma_{L,1}^A, \gamma_{L,2}^B, \gamma_{R,1}^A, \gamma_{R,2}^B)_\gamma^T$ will allow us to identify this matrix \mathcal{H}_0 with the effective subgap Hamiltonian (A1). Indeed, writing

the ψ^γ basis states in terms of ψ^0 components,

$$\begin{aligned} (1 \ 0 \ 0 \ 0)_\gamma^T &\equiv \frac{1}{\sqrt{2}}(1 \ 0 \ 1 \ 0)_0^T, & (0 \ 1 \ 0 \ 0)_\gamma^T &\equiv \frac{1}{\sqrt{2}}(-i \ 0 \ i \ 0)_0^T, \\ (0 \ 0 \ 1 \ 0)_\gamma^T &\equiv \frac{1}{\sqrt{2}}(0 \ 1 \ 0 \ 1)_0^T, & (0 \ 0 \ 0 \ 1)_\gamma^T &\equiv \frac{1}{\sqrt{2}}(0 \ -i \ 0 \ i)_0^T, \end{aligned} \quad (\text{A8})$$

we can express the Hamiltonian \mathcal{H}_0 in this new basis as

$$(\mathcal{H}_\gamma)_{ij} = \langle \psi_i^\gamma | \mathcal{H}_0 | \psi_j^\gamma \rangle, \quad (\text{A9})$$

which yields

$$\begin{aligned} H_\gamma &= \frac{1}{2} \sum_{ij} \psi_i^{\gamma\dagger} (\mathcal{H}_\gamma)_{ij} \psi_j^\gamma \\ &= \frac{i}{2} \psi^{\gamma\dagger} \begin{pmatrix} 0 & \frac{\mu_{L,1}\mu_{L,2} - (t_L + \Delta_L)(t_L - \Delta_L)}{t_L + \Delta_L} & -\frac{t_J \mu_{L,1} \sin \frac{\phi}{2}}{t_L + \Delta_L} & -\frac{t_J \mu_{L,1} \mu_{R,2} \cos \frac{\phi}{2}}{(t_L + \Delta_L)(t_R + \Delta_R)} \\ \frac{(t_L + \Delta_L)(t_L - \Delta_L) - \mu_{L,1}\mu_{L,2}}{t_L + \Delta_L} & 0 & t_J \cos \frac{\phi}{2} & -\frac{t_J \mu_{R,2} \sin \frac{\phi}{2}}{t_R + \Delta_R} \\ \frac{t_J \mu_{L,1} \sin \frac{\phi}{2}}{t_L + \Delta_L} & -t_J \cos \frac{\phi}{2} & 0 & \frac{\mu_{R,1}\mu_{R,2} - (t_R + \Delta_R)(t_R - \Delta_R)}{t_R + \Delta_R} \\ \frac{t_J \mu_{L,1} \mu_{R,2} \cos \frac{\phi}{2}}{(t_L + \Delta_L)(t_R + \Delta_R)} & \frac{t_J \mu_{R,2} \sin \frac{\phi}{2}}{t_R + \Delta_R} & \frac{(t_R + \Delta_R)(t_R - \Delta_R) - \mu_{R,1}\mu_{R,2}}{t_R + \Delta_R} & 0 \end{pmatrix} \psi^\gamma. \end{aligned} \quad (\text{A10})$$

Therefore, we can identify each element of this matrix with one coefficient $\lambda_{\alpha\beta}$ of Eq. (A1). This effective Hamiltonian contains three different contributions: (i) terms $\sim \cos(\phi/2)$ and $\sim \sin(\phi/2)$ are interchain Majorana couplings $\{\gamma_{L,2}^B \leftrightarrow \gamma_{R,1}^A, \gamma_{L,1}^A \leftrightarrow \gamma_{R,2}^B\}$ and $\{\gamma_{L,1}^A \leftrightarrow \gamma_{R,1}^A, \gamma_{L,2}^B \leftrightarrow \gamma_{R,2}^B\}$, respectively, whereas (ii) ϕ -independent terms are intrachain couplings $\{\gamma_{L,1}^A \leftrightarrow \gamma_{L,2}^B, \gamma_{R,1}^A \leftrightarrow \gamma_{R,2}^B\}$. As we will see in Appendix A 3—Eq. (A16)—the intercouplings $\sim \sin(\phi/2)$ will give rise to an off-diagonal contribution acting on the pseudospin parity space additional to the term $E_M \cos(\phi/2)$ usually found in the literature. It should also be noted that this low-energy projection is an approximation: the separation between bulk and subgap contributions is only well-defined if the subgap modes are well-detached from the quasicontinuum.

2. Comparison between eight and four Majoranas

Since our main objective is to study the physics of a superconducting qubit modified by the presence of the DQD Josephson junction, we first check the limitations of the effective Josephson potential obtained previously. At this level, it is enough to compare results from the projected potential in Eq. (A10) with the phase-dependent energy spectrum $E(\phi)$ of the BdG form of the full Hamiltonian $H_{\text{BdG}}^{\text{JJ}}$ before any projection, Fig. 5. At the sweet spot [$\Delta = t$, $\mu_E = \mu_I = 0$, Fig. 5(a)], the subgap spectrum shows a 4π Josephson effect indicating the presence of Majorana zero modes (thin gray lines). This spectrum originates from the fusion (energy splitting) of the inner MBSs living in the junction $\gamma_{L,2}^B$ and $\gamma_{R,1}^A$ (which is maximum at $\phi = 0, 2\pi$), but without breaking the degeneracy point at $\phi = \pi$. Moreover, two states remain at zero energy for all phases, corresponding to the Majorana states $\gamma_{L,1}^A$ and $\gamma_{R,2}^B$ living in the outermost quantum dots. In this regime, both the full solution (left panel) and the four MBSs projection (right panel) coincide. Of course, the latter does not capture the bulk solutions that disperse

with phase near $2\Delta = 2t$. Deviations from the sweet spot by changing the internal chemical potential $\mu_I \neq 0$ do not affect the low-energy spectrum but open gaps in the bulk (colored lines). When moving away from the sweet spot by tuning the external chemical potentials $\mu_E \neq 0$, while keeping $\mu_I = 0$, the spectrum remains 4π -periodic. In this case, the low-energy states are lifted away from zero energy, Fig. 5(b) (blue/green colored lines), resulting in a characteristic diamondlike shape. The crossings forming the diamonds become avoided crossings for $\mu_I \neq 0$ and $\mu_E \neq 0$, Fig. 5(c), which also splits the crossings of the bulk bands near $\phi = \pi$, giving an overall 2π -periodic spectrum. In contrast, a zero-energy state persists for $\mu_E = 0$ and independently from μ_I , even at large values, Fig. 5(d), corresponding to the Majorana states of the outermost dots having zero weight in the inner ones. In this regime, the effect of detuning μ_I away from the sweet spot only affects the localization of the inner Majorana state, decreasing the splitting between the blue states, and resulting in a robust 4π -periodic spectrum.

In all the cases described above, the approximation derived in Eq. (A10) using four Majorana states describes well the low-energy states of the system close to the sweet spot. In contrast, this approximation largely deviates from the results of the full Hamiltonian for sufficiently large $\mu_E \gtrsim \Delta$ and irrespective of μ_I , Figs. 5(e) and 5(f). In this regime, the bulk solutions that appear at $E \sim 2\Delta$ at the sweet spot hybridize with the low-energy states, renormalizing their energy and strongly affecting their dispersion against phase. Therefore, the low-energy states cannot be described by only four Majorana states (one per dot).

We demonstrate the importance of considering all the Majorana states in every dot by calculating the real space-resolved distribution of the wave functions, taken as the probability $P_j(\gamma_{\alpha,i}^{A/B}) = \langle \psi_j | \Psi_{\alpha,i}^{A/B} \rangle \langle \Psi_{\alpha,i}^{A/B} | \psi_j \rangle$ of the eigenstate $|\psi_j\rangle$ of $H_{\text{BdG}}^{\text{JJ}}$ on each mode $\gamma_{\alpha,i}^{A/B}$, represented in the Majorana basis (A4). Here indices $i = 1, 2$ and $\alpha = L, R$ denote the sites of each chain, whereas $j = \text{green, blue}$ labels the different

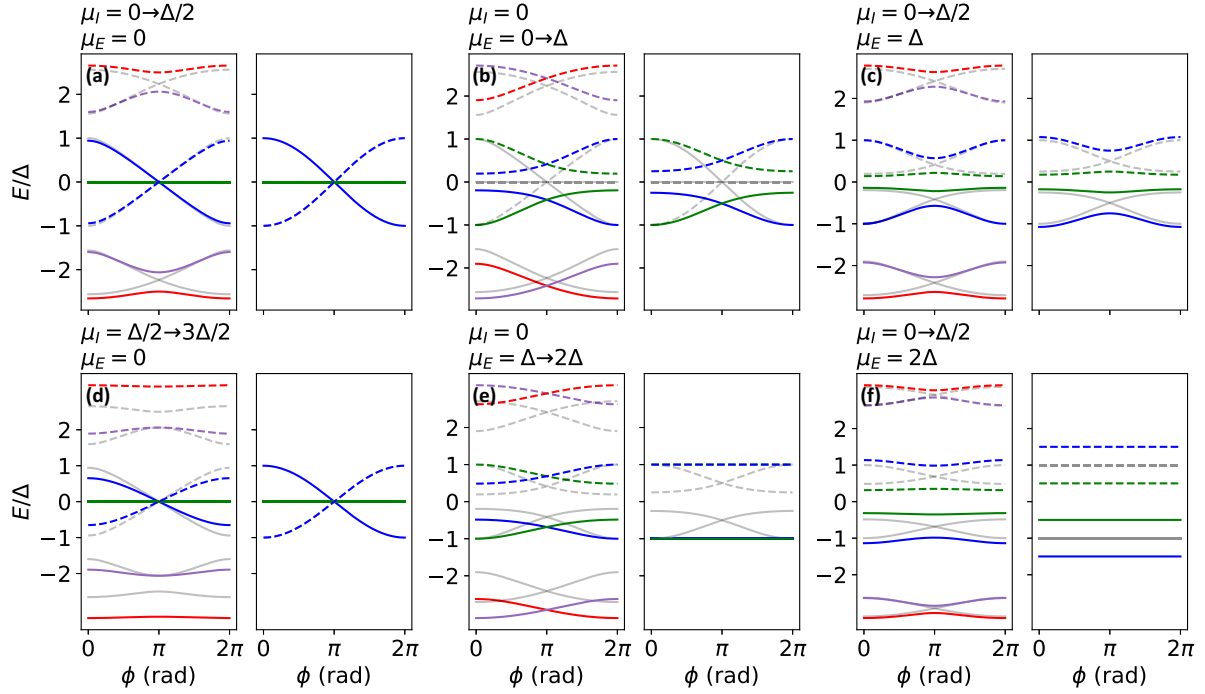


FIG. 5. Evolution of the energy spectrum as a function of ϕ for the parameter trajectory indicated in each panel. In each case, the leftmost panels correspond to the BdG form of the full Hamiltonian—Eqs. (1) and (2) using the Majorana spinor (3) of the main text—and the rightmost panels to the four Majoranas projection—Eq. (A10). Gray/colored levels denote the beginning/end of each trajectory. We have fixed $t_J = t = \Delta$ for every panel.

levels that appear in Fig. 5. As we can see in Fig. 6, at the sweet spot the outermost Majoranas are pinned to zero energy (green states in Fig. 5), whereas (oscillating) blue states correspond to innermost Majoranas at $\phi = 0$. Starting from this point, varying ϕ causes the blue states to delocalize along the junction. A similar behavior is found on the green states with variations of μ_E outside the sweet spot. Changing t_J , however, does not cause any change in the wave functions of the subgap states.

The fact that the eigenstates of the system have non-negligible values outside the low-energy subspace points to a limitation of the projection performed in the previous section, which is only valid close to the sweet spot. As we discuss in what follows, a low-energy subspace that is written in terms of many-body occupations (even and odd) of the system is much more powerful. Starting first from the four Majoranas projection written in the many-body fermionic occupation basis (Appendix A 3), we obtain the corresponding subgap Josephson potential [Eq. (5) in the main text]. In Appendix B, we go beyond this picture and describe the effective low-energy physics of the problem in terms of total many-body occupations including contributions from the four QDs (eight MBSs) forming the Josephson junction, which allows us to obtain a subgap Josephson potential that includes terms containing both μ_E and μ_I on an equal footing and to all orders [Eq. (8) of the main text].

3. Projection in the left/right fermionic parity basis

We can now write the matrix elements of $V_{\text{DQD}}^{\text{JJ}}$ in the fermionic parity basis $|n_L, n_R\rangle$. For the total even-parity state,

the effective Josephson coupling reads

$$V_{\text{DQD}}^{\text{JJ}} = \begin{pmatrix} \langle 00|H_\gamma|00\rangle & \langle 00|H_\gamma|11\rangle \\ \langle 11|H_\gamma|00\rangle & \langle 11|H_\gamma|11\rangle \end{pmatrix}. \quad (\text{A11})$$

Since the parity states are defined such that (similar for c_R, c_R^\dagger)

$$\begin{aligned} c_L^\dagger |n_L, n_R\rangle &= \sqrt{n_L + 1} |n_L + 1, n_R\rangle, \\ c_L |n_L, n_R\rangle &= \sqrt{n_L} |n_L - 1, n_R\rangle, \\ \hat{n}_L |n_L, n_R\rangle &= c_L^\dagger c_L |n_L, n_R\rangle = n_L |n_L, n_R\rangle, \end{aligned} \quad (\text{A12})$$

and attending to the decomposition of these fermionic operators in Majorana operators (A2), we can write the following operations:

$$\begin{aligned} i\gamma_{\alpha,1}^A \gamma_{\alpha,2}^B |00/11\rangle &= -/ + |00/11\rangle, \\ \gamma_{L,1}^A \gamma_{R,1}^A |00/11\rangle &= -/ + |11/00\rangle, \\ i\gamma_{L,1}^A \gamma_{R,2}^B |00/11\rangle &= |11/00\rangle, \\ i\gamma_{L,2}^B \gamma_{R,1}^A |00/11\rangle &= |11/00\rangle, \\ \gamma_{L,2}^B \gamma_{R,2}^B |00/11\rangle &= +/- - |11/00\rangle. \end{aligned} \quad (\text{A13})$$

Therefore, the subgap contribution written in the even fermionic parity basis is

$$\begin{aligned} \langle 00|H_\gamma|00\rangle &= -(\lambda_{L1,L2} + \lambda_{R1,R2}), \\ \langle 11|H_\gamma|11\rangle &= \lambda_{L1,L2} + \lambda_{R1,R2}, \\ \langle 00|H_\gamma|11\rangle &= i\lambda_{L1,R1} + \lambda_{L1,R2} + \lambda_{L2,R1} - i\lambda_{L2,R2}, \\ \langle 11|H_\gamma|00\rangle &= -i\lambda_{L1,R1} + \lambda_{L1,R2} + \lambda_{L2,R1} + i\lambda_{L2,R2}, \end{aligned} \quad (\text{A14})$$

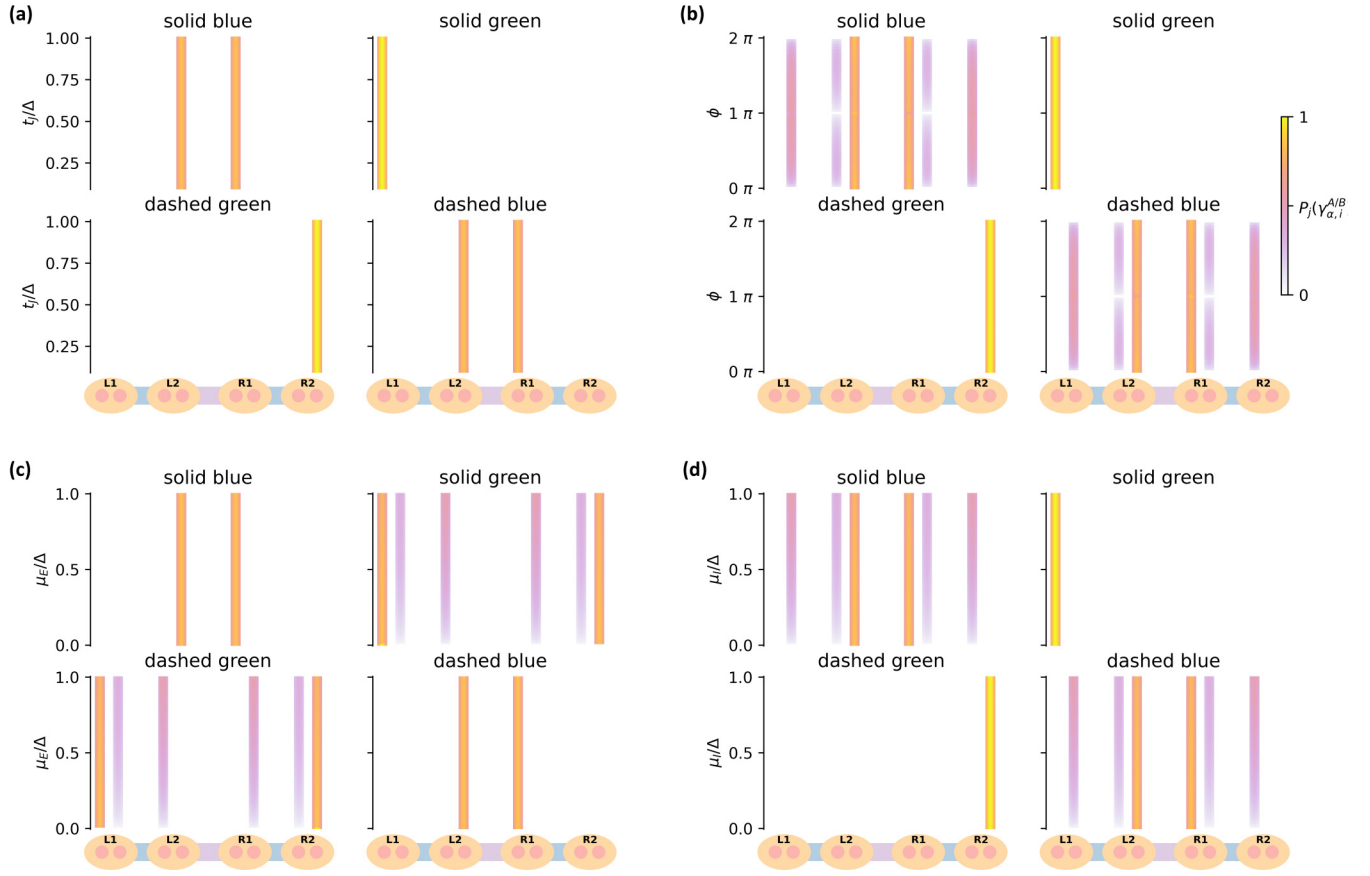


FIG. 6. Evolution of the space distribution of subgap states as a function of (a) t_J with $\mu_E = \mu_I = 0$ and $\phi = 0$; (b) ϕ with $\mu_E = \mu_I = 0$; (c) μ_E with $\mu_I = 0$ and $\phi = 0$; and (d) μ_I with $\mu_E = 0$ and $\phi = 0$. We have fixed $\Delta = t = t_J$ for all panels, and subtitles refer to each eigenstate plotted in Fig. 5.

where $\lambda_{\alpha\beta}$ are the matrix elements of (A10). Finally, the subgap Josephson potential takes the form

$$V_{\text{DQD}}^{\text{JJ}}(\phi) = \frac{1}{2} \left(t_J \left(1 - \frac{\mu_{L,1}\mu_{R,2}}{(t+\Delta)^2} \right) \cos \frac{\phi}{2} + it_J \frac{\mu_{L,1} - \mu_{R,2}}{t+\Delta} \sin \frac{\phi}{2} \right) \frac{t_J \left(1 - \frac{\mu_{L,1}\mu_{R,2}}{(t+\Delta)^2} \right) \cos \frac{\phi}{2} - it_J \frac{\mu_{L,1} - \mu_{R,2}}{t+\Delta} \sin \frac{\phi}{2}}{\frac{(\mu_{L,1}\mu_{L,2} + \mu_{R,1}\mu_{R,2}) - 2(t+\Delta)(t-\Delta)}{t+\Delta}}. \quad (\text{A15})$$

Therefore, we can split this subgap effective potential in three different terms acting on a pseudospin parity space [Eq. (4) of the main text],

$$V_{\text{DQD}}^{\text{JJ}}(\phi) = E_M \cos \frac{\phi}{2} \sigma_x + E_M^S \sin \frac{\phi}{2} \sigma_y + \lambda \sigma_z, \quad E_M = \frac{t_J}{2} \left(1 - \frac{\mu_{L,1}\mu_{R,2}}{(t+\Delta)^2} \right),$$

$$E_M^S = t_J \frac{\mu_{L,1} - \mu_{R,2}}{2(t+\Delta)}, \quad \lambda = \frac{2(t+\Delta)(t-\Delta) - (\mu_{L,1}\mu_{L,2} + \mu_{R,1}\mu_{R,2})}{2(t+\Delta)}. \quad (\text{A16})$$

It is straightforward to see that, when restricting ourselves to the symmetric case $\mu_{L,1} = \mu_{R,2} = \mu_E$ and $\mu_{L,2} = \mu_{R,1} = \mu_I$, the Josephson potential reduces to Eq. (5) of the main text.

APPENDIX B: BEYOND THE FOUR MAJORANAS PROJECTION: PROJECTION ONTO A FULL MANY-BODY PARITY BASIS

A reasonable alternative treatment of the problem is to choose as our new fermionic parity subspace the two lowest-energy many-body eigenstates $\{|O_L^-, O_R^-\rangle, |E_L^-, E_R^-\rangle\}$ of both chains isolated from each other ($t_J = 0$), where

$$H_\alpha = \begin{pmatrix} 0 & 0 & 0 & \Delta_\alpha \\ 0 & -\mu_{\alpha,1} & -t_\alpha & 0 \\ 0 & -t_\alpha & -\mu_{\alpha,2} & 0 \\ \Delta_\alpha & 0 & 0 & -(\mu_{\alpha,1} + \mu_{\alpha,2}) \end{pmatrix} \quad (\text{B1})$$

is the many-body Hamiltonian of one chain in the basis of occupation states $\{|00\rangle, |10\rangle, |01\rangle, |11\rangle\}$. Defining $\mu_\alpha = (\mu_{\alpha,1} + \mu_{\alpha,2})/2$ and $\delta_\alpha = (\mu_{\alpha,1} - \mu_{\alpha,2})/2$, its eigenstates and eigenenergies are

$$\begin{aligned} |O_\alpha^-\rangle &= (0, \Psi_{\alpha,1}^A, \Psi_{\alpha,1}^B, 0)^T \propto \left(0, \frac{2\delta_\alpha + \epsilon_{\alpha O}^+ - \epsilon_{\alpha O}^-}{2t_\alpha}, 1, 0\right)^T, & \epsilon_{\alpha O}^- &= -\mu_\alpha - \sqrt{t_\alpha^2 + \delta_\alpha^2}, \\ |O_\alpha^+\rangle &= (0, \Psi_{\alpha,2}^A, \Psi_{\alpha,2}^B, 0)^T \propto \left(0, \frac{2\delta_\alpha - \epsilon_{\alpha O}^+ + \epsilon_{\alpha O}^-}{2t_\alpha}, 1, 0\right)^T, & \epsilon_{\alpha O}^+ &= -\mu_\alpha + \sqrt{t_\alpha^2 + \delta_\alpha^2}, \\ |E_\alpha^-\rangle &= (\Psi_{\alpha,3}^A, 0, 0, \Psi_{\alpha,3}^B)^T \propto \left(\frac{-\epsilon_{\alpha E}^+}{\Delta_\alpha}, 0, 0, 1\right)^T, & \epsilon_{\alpha E}^- &= -\mu_\alpha - \sqrt{\Delta_\alpha^2 + \mu_\alpha^2}, \\ |E_\alpha^+\rangle &= (\Psi_{\alpha,4}^A, 0, 0, \Psi_{\alpha,4}^B)^T \propto \left(\frac{-\epsilon_{\alpha E}^-}{\Delta_\alpha}, 0, 0, 1\right)^T, & \epsilon_{\alpha E}^+ &= -\mu_\alpha + \sqrt{\Delta_\alpha^2 + \mu_\alpha^2}. \end{aligned} \quad (\text{B2})$$

To construct the Hamiltonian of the junction living in the bipartite Hilbert space $\mathcal{H}_L \otimes \mathcal{H}_R$, we represent it on the basis of joint eigenstates $\{|i_L, j_R\rangle = |i_L\rangle \otimes |j_R\rangle\}$ with $i, j = O^\pm, E^\pm$. Thus, the Hamiltonian $\tilde{H}_{\text{DQD}}^{\text{JJ}} = \tilde{H}_L + \tilde{H}_R + \tilde{H}_J$ has a diagonal term

$$\tilde{H}_L + \tilde{H}_R = (P_L^{-1} H_L P_L) \otimes \mathbb{I}_R + \mathbb{I}_L \otimes (P_R^{-1} H_R P_R) = \text{diag}(\epsilon_{LO}^-, \epsilon_{LO}^+, \epsilon_{LE}^-, \epsilon_{LE}^+) \otimes \mathbb{I}_R + \mathbb{I}_L \otimes \text{diag}(\epsilon_{RO}^-, \epsilon_{RO}^+, \epsilon_{RE}^-, \epsilon_{RE}^+), \quad (\text{B3})$$

where P_α is the change-of-basis matrix onto the eigenbasis of each chain. On the other hand, the off-diagonal term \tilde{H}_J is due to the Josephson tunneling between both chains, which can be easily represented on the joint-occupation basis $\{|n_{L,1}, n_{L,2}\rangle \otimes |n_{R,1}, n_{R,2}\rangle\}_{n_{\alpha,i}=0,1}$ and then projected onto the eigenbasis by the change-of-basis matrix $P_{LR} = P_L \otimes P_R$.

Finally, the Josephson potential (ignoring higher-order contributions from the rest of the eigenstates) can be written as

$$\begin{aligned} V_{\text{DQD}}^{\text{JJ}} &= \begin{pmatrix} \langle O_L^-, O_R^- | \tilde{H}_{\text{DQD}}^{\text{JJ}} | O_L^-, O_R^- \rangle & \langle O_L^-, O_R^- | \tilde{H}_{\text{DQD}}^{\text{JJ}} | E_L^-, E_R^- \rangle \\ \langle E_L^-, E_R^- | \tilde{H}_{\text{DQD}}^{\text{JJ}} | O_L^-, O_R^- \rangle & \langle E_L^-, E_R^- | \tilde{H}_{\text{DQD}}^{\text{JJ}} | E_L^-, E_R^- \rangle \end{pmatrix}, \\ \langle O_L^-, O_R^- | \tilde{H}_{\text{DQD}}^{\text{JJ}} | O_L^-, O_R^- \rangle &= \epsilon_{LO}^- + \epsilon_{RO}^-, & \langle E_L^-, E_R^- | \tilde{H}_{\text{DQD}}^{\text{JJ}} | E_L^-, E_R^- \rangle &= \epsilon_{LE}^- + \epsilon_{RE}^+, \\ \langle E_L^-, E_R^- | \tilde{H}_{\text{DQD}}^{\text{JJ}} | O_L^-, O_R^- \rangle &= t_J \left(4t^2 \sqrt{\frac{\epsilon_{RE}^+}{\epsilon_{LE}^+}} e^{i\phi/2} + \sqrt{\frac{\epsilon_{LE}^+}{\epsilon_{RE}^+}} (2\delta_L + \epsilon_{LO}^- - \epsilon_{LO}^+) (2\delta_R + \epsilon_{RO}^- - \epsilon_{RO}^+) e^{-i\phi/2} \right) \\ &\times \frac{\Delta \sqrt{(2\delta_L + \epsilon_{LO}^+ - \epsilon_{LO}^-)(2\delta_R + \epsilon_{RO}^+ - \epsilon_{RO}^-)}}{8t^2 \sqrt{(\epsilon_{LO}^+ - \epsilon_{LO}^-)(\epsilon_{RO}^+ - \epsilon_{RO}^-)(\epsilon_{LE}^+ - \epsilon_{LE}^-)(\epsilon_{RE}^+ - \epsilon_{RE}^-)}} \\ &= -t_J \Psi_{L,1}^A \Psi_{R,1}^A \left(\Psi_{L,3}^B \Psi_{R,3}^A e^{i\phi/2} - \Psi_{L,4}^B \Psi_{R,4}^A \frac{\Psi_{L,2}^A \Psi_{R,2}^A}{\Psi_{L,2}^B \Psi_{R,2}^B} e^{-i\phi/2} \right). \end{aligned} \quad (\text{B4})$$

One can see that if the chemical potentials are constrained to the special symmetric choice $\mu_{L,1} = \mu_{R,2} = \mu_E$ and $\mu_{L,2} = \mu_{R,1} = \mu_I$ (external versus internal), such that $\mu_L = \mu_R = (\mu_E + \mu_I)/2 = \mu$ and $\delta_L = -\delta_R = (\mu_E - \mu_I)/2 = \delta$, and considering $\Delta_L = \Delta_R$ and $t_L = t_R$, this Josephson potential reduces to the simpler form [Eq. (7) of the main text]

$$V_{\text{DQD}}^{\text{JJ}}(\phi) = \begin{pmatrix} -2\mu - 2\sqrt{t^2 + \delta^2} & \frac{t_J \Delta t}{2\sqrt{(t^2 + \delta^2)(\Delta^2 + \mu^2)}} \cos(\phi/2) \\ \frac{t_J \Delta t}{2\sqrt{(t^2 + \delta^2)(\Delta^2 + \mu^2)}} \cos(\phi/2) & -2\mu - 2\sqrt{\Delta^2 + \mu^2} \end{pmatrix}. \quad (\text{B5})$$

Moreover, asymmetries in CAR and ECT amplitudes between left and right chains could arise in an experimental realization of the device. However, we can demonstrate that all the physics of the MW response presented in this work remain true at the sweet spot ($\forall \mu_{\alpha,i} = 0, t_\alpha = \Delta_\alpha$), but with different t_L and t_R . Indeed, when all the chemical potentials are tuned to zero, E_M is independent of t_α and the diagonal terms of the Josephson potential are equivalent to the symmetric case:

$$V_{\text{DQD}}^{\text{JJ}}(\phi) = \begin{pmatrix} -t_L - t_R & \frac{t_J}{2} \cos(\phi/2) \\ \frac{t_J}{2} \cos(\phi/2) & -\Delta_L - \Delta_R \end{pmatrix}. \quad (\text{B6})$$

Hence, the spectral hole shown in Fig. 4 of the main text will arise at the sweet spot although $t_L \neq t_R$, as a clear signature of the 4π -Josephson effect. Furthermore, the exact $1e$ shift in n_g going from the ECT-dominated regime to the CAR-dominated regime will also appear, as the diagonal splitting between the even and odd states does not depend on the coupling strengths in each single chain, but the global ratio $(t_L + t_R)/(\Delta_L + \Delta_R)$. Finally, note that the possibility of extracting E_M from the qubit frequency ω_{KIT} in the transmon regime is a universal prediction that remains true for any configuration of the parameters of the device.

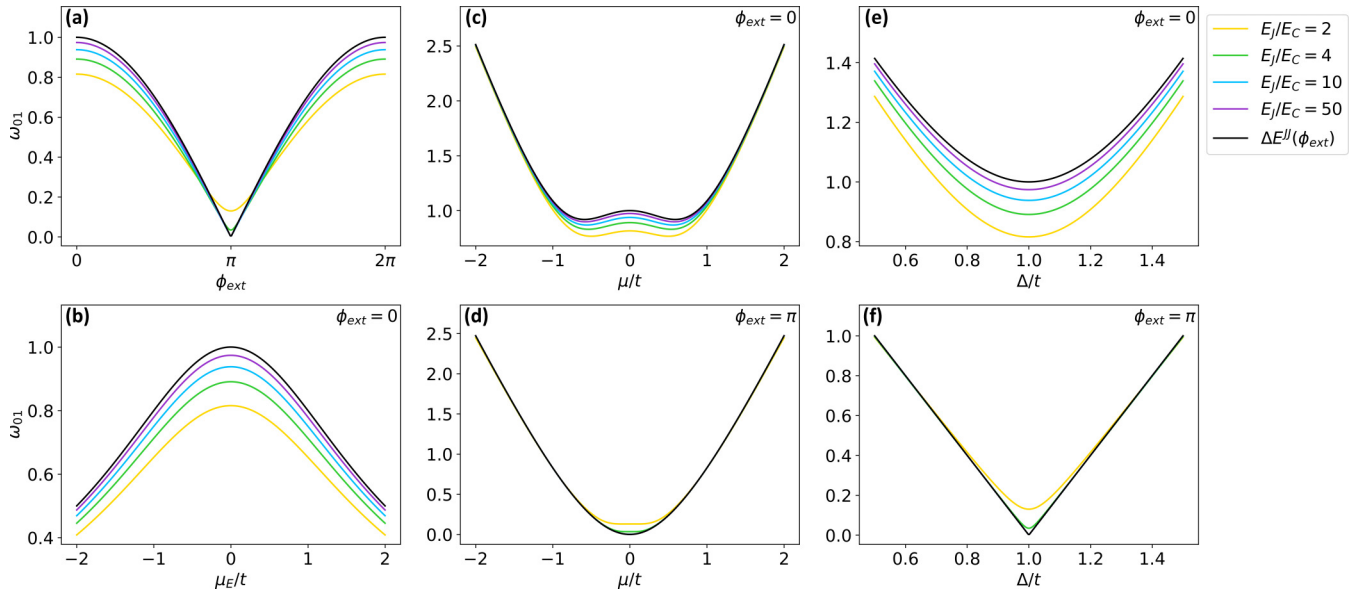


FIG. 7. Transition frequency ω_{01} for $E_J/E_C = 2, 4, 10, 50$, compared to analytical result (D1), black line, as a function of (a) ϕ_{ext} at the sweet spot; (b) μ_E with $\mu_I = 0$, $\Delta = t$, and $\phi_{\text{ext}} = 0$; (c),(d) $\mu_E = \mu_I = \mu$ with $\Delta = t$ and $\phi_{\text{ext}} = 0, \pi$, respectively; and (e),(f) Δ/t with $\mu_E = \mu_I = 0$ and $\phi_{\text{ext}} = 0, \pi$, respectively. We have fixed $t_J/t = 1$ for all panels.

APPENDIX C: MAJORANA POLARIZATION

The Hamiltonian H^{JJ} described above can be separated into two independent blocks of even ($\{|O_L^\pm, O_R^\pm\rangle, |E_L^\pm, E_R^\pm\rangle\}$) and odd ($\{|E_L^\pm, O_R^\pm\rangle, |O_L^\pm, E_R^\pm\rangle\}$) total parity, which leads to a twofold-degenerate spectrum. To determine whether these degeneracies are associated with MBSs, we use the Majorana polarization (MP). This magnitude quantifies the MBS quality and is defined as the degree that a Hermitian operator localized on one of the quantum dots can switch between the lowest-energy states of even and odd blocks,

$$\begin{aligned} \text{MP}_{\alpha,i} &= \frac{w_{\alpha,i}^2 - z_{\alpha,i}^2}{w_{\alpha,i}^2 + z_{\alpha,i}^2}, & w_{\alpha,i} &= \langle O | c_{\alpha,i} + c_{\alpha,i}^\dagger | E \rangle, \\ z_{\alpha,i} &= \langle O | c_{\alpha,i} - c_{\alpha,i}^\dagger | E \rangle. \end{aligned} \quad (\text{C1})$$

We can see that, for $t_J = 0$, MP can be written as

$$\text{MP}_{\alpha,i} = \frac{t_\alpha \Delta_\alpha}{(-1)^{i+1} \delta_\alpha \mu_\alpha - \sqrt{(t_\alpha^2 + \delta_\alpha^2)(\Delta_\alpha^2 + \mu_\alpha^2)}}, \quad (\text{C2})$$

where $|E\rangle = |O_L^-, O_R^-\rangle$, $|O\rangle_{\alpha=L} = |E_L^-, O_R^-\rangle$, $|O\rangle_{\alpha=R} = |O_L^-, E_R^-\rangle$. Restricting ourselves to $t_\alpha = \Delta_\alpha$, $|\text{MP}_{\alpha,1}|$ ($|\text{MP}_{\alpha,2}|$) is maximum when $\mu_\alpha = \delta_\alpha$ ($\mu_\alpha = -\delta_\alpha$), that is, when $\mu_{\alpha,2} = 0$ ($\mu_{\alpha,1} = 0$).

Furthermore, from (B5), the effective Majorana coupling E_M is related to this quantity such that

$$E_M = \frac{-t_J \text{MP}_{\alpha,i}/2}{1 + (-1)^{i+\alpha} \frac{\delta_\alpha \mu_\alpha}{t_\alpha} \text{MP}_{\alpha,i}}, \quad (\text{C3})$$

where $\alpha = \{0 \equiv L, 1 \equiv R\}$. Thus, if $\mu_E = \mu_I$ ($\mu_E = -\mu_I$), that is, $\delta = 0$ ($\mu = 0$), then E_M is proportional to MP: $E_M = -t_J \text{MP}/2$.

APPENDIX D: INTRABAND SPLITTING IN TRANSMON REGIME

At $n_g = 0.25$, the energy splitting between the ground state and the first excited state is merely due to the subgap Josephson potential since the rest of the terms on the qubit Hamiltonian give rise to a doubly degenerate state at this point. Hence, it is reasonable to express the Kitmon qubit frequency $\omega_{\text{KIT}} \equiv \omega_{01}$ as the difference between the two eigenvalues of $V_{\text{DQD}}^{\text{JJ}}(\phi)$,

$$\Delta E^{\text{JJ}}(\phi) = 2\sqrt{(\sqrt{t^2 + \delta^2} - \sqrt{\Delta^2 + \mu^2})^2 + E_M^2 \cos^2 \frac{\phi}{2}}. \quad (\text{D1})$$

As we can see, this difference depends on ϕ and, hence, one should know the explicit form of the qubit wave functions to relate this quantity to ω_{01} . Nevertheless, in the deep transmon regime ($E_J/E_C \gg 1$) these eigenfunctions can be approximated to harmonic-oscillator states sharpened around ϕ_{ext} , so that the Kitmon frequency is $\omega_{\text{KIT}} \approx \Delta E^{\text{JJ}}(\phi_{\text{ext}})$ —Eq. (12) of the main text. Likewise, in the transmon regime the qubit spectrum is insensitive to changes in the charge offset n_g , this approximation being valid for every parametric configuration of the system, even when diagonal terms of $V_{\text{DQD}}^{\text{JJ}}(\phi)$ are not equal and these avoided crossings do not occur at $n_g = 0.25$ in the charging regime.

Figure 7 displays the transition frequency $\omega_{01}(n_g = 0.25)$ as a function of different parameters, showing their evolution with increasing E_J/E_C ratios. We show the convergence to $\Delta E^{\text{JJ}}(\phi_{\text{ext}})$ in the limit $E_J/E_C \gg 1$.

We can also check this approximation numerically by calculating the distance between the curves that the analytical result (D1) and ω_{01} trace for increasing E_J/E_C ratios. The distance between two curves described by the functions $f(x)$

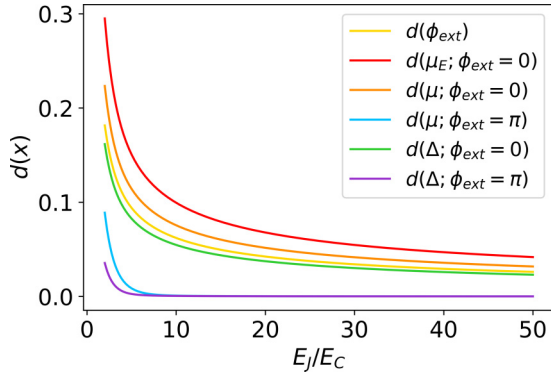


FIG. 8. Distance between curves ω_{01} and $\Delta E^{JJ}(\phi_{\text{ext}})$ as a function of E_J/E_C for the same curves shown in Fig. 7 (see the legend).

and $g(x)$ over a parametric trajectory $x \in \mathcal{X}$ is written as

$$d(f, g) = \left(\int_{\mathcal{X}} dx |f(x) - g(x)|^2 \right)^{1/2}. \quad (\text{D2})$$

As we can observe in Fig. 8, increasing the ratio E_J/E_C minimizes the distance between numerical results and our analytical approximation, which allows us to predict ω_{KIT} with great precision in the deep transmon regime.

Finally, we include some additional results that show a full progression of the energy spectrum and its MW response for increasing E_J/E_C ratios. In particular, we can see in Fig. 9 an enhancement of the insensitivity to the charge offset as the qubit enters the transmon regime, with a dominant transition ω_{02} . Furthermore, Fig. 10 shows how the spectral hole in ω_{02} at ϕ_{ext} narrows until true energy crossing appears as the E_J/E_C ratio increases.

APPENDIX E: NUMERICAL METHODS FOR THE MAJORANA-TRANSMON QUBIT: TIGHT-BINDING TREATMENT

1. Phase space

In phase space, the numerical solution of the qubit Hamiltonian

$$H_Q = 4E_C(\hat{n} - n_g)^2 + V_J(\phi) \quad (\text{E1})$$

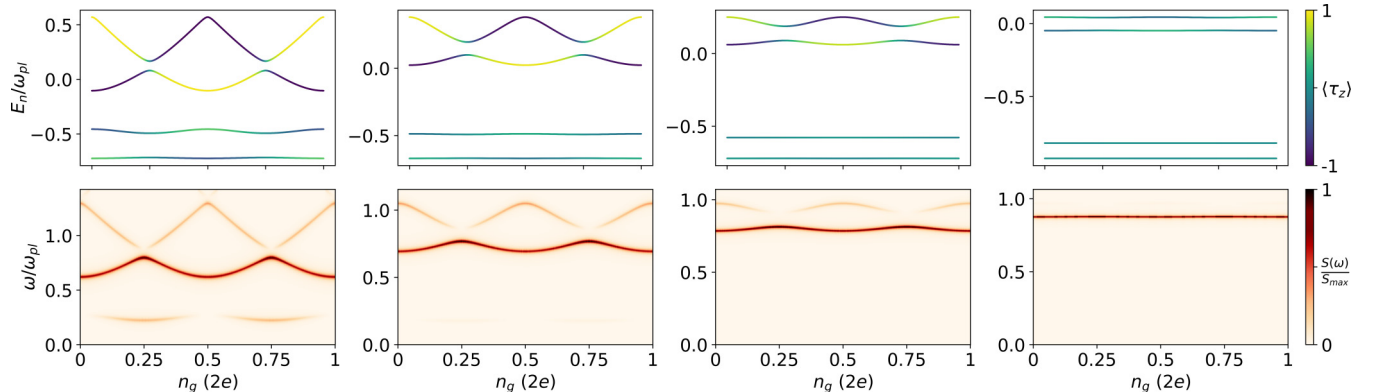


FIG. 9. Full evolution of the energy spectrum and its MW response as a function of n_g at the sweet spot ($\phi_{\text{ext}} = 0$) for $E_J/E_C = 1.5, 3, 5, 10$ (from left to right).

is accomplished by discretizing the phase space as $\phi_j = 2\pi j/l^\phi$, with $j = 1, \dots, l^\phi$, defining a set of sites arranged into a circular chain. In so doing, the Hamiltonian acquires a tight-binding form and it allows us to define a finite fermionic Hilbert space and operators b_j^\dagger such that their action on the ground state is $b_j^\dagger|0\rangle = \Psi(\phi_j)$, where $\Psi(\phi)$ is the eigenstate at phase ϕ .

Then, starting from the definition of the derivative

$$\frac{df(x)}{dx} = \lim_{h \rightarrow 0} \frac{f(x+h) - f(x-h)}{2h}, \quad (\text{E2})$$

we can express the operator $\hat{n} = -i\partial_\phi$ in the discretized form

$$-i\partial_\phi = -i \frac{(b_{i+1}^\dagger - b_{i-1}^\dagger)b_i}{2a_\phi}, \quad (\text{E3})$$

where $a_\phi = 2 \sin(\pi/l^\phi)$ is a phase lattice constant. By construction, the second derivative is defined as

$$\frac{d^2 f(x)}{dx^2} = \lim_{h \rightarrow 0} \frac{f(x+h) - 2f(x) + f(x-h)}{h^2}, \quad (\text{E4})$$

so we can write

$$\partial_\phi^2 = \frac{(b_{i+1}^\dagger - 2b_i^\dagger + b_{i-1}^\dagger)b_i}{a_\phi^2}. \quad (\text{E5})$$

Hence, the Hamiltonian (E1) reads

$$\begin{aligned} H &= \sum_j b_j^\dagger h_j^\phi b_j + \sum_{(j,k)} b_j^\dagger v_{jk}^\phi b_k, \\ h_j^\phi &= 4E_C(2a_\phi^{-2} + n_g^2) + V_J(\phi_j), \\ v_{jk}^\phi &= 4E_C[\text{sgn}(j-k)in_g a_\phi^{-1} - a_\phi^{-2}], \end{aligned} \quad (\text{E6})$$

where each site element h_j^ϕ, v_{jk}^ϕ is a 2×2 matrix, due to the pseudospin structure from even-odd projection.

Secondly, the eigenstates of the Hamiltonian (E1) are defined as a two-component spinor $\Psi_k = (f_k(\phi), g_k(\phi))^T$ with periodic/antiperiodic boundary conditions in phase space, $f(\phi + 2\pi) = f(\phi)$ and $g(\phi + 2\pi) = -g(\phi)$, due to their even/odd fermionic parity. To make the Hamiltonian fully periodic, it is rotated according to $H(\phi) \rightarrow UH(\phi)U^\dagger$, with $U = \text{diag}(1, e^{i\phi/2})$. Therefore, the final form of the

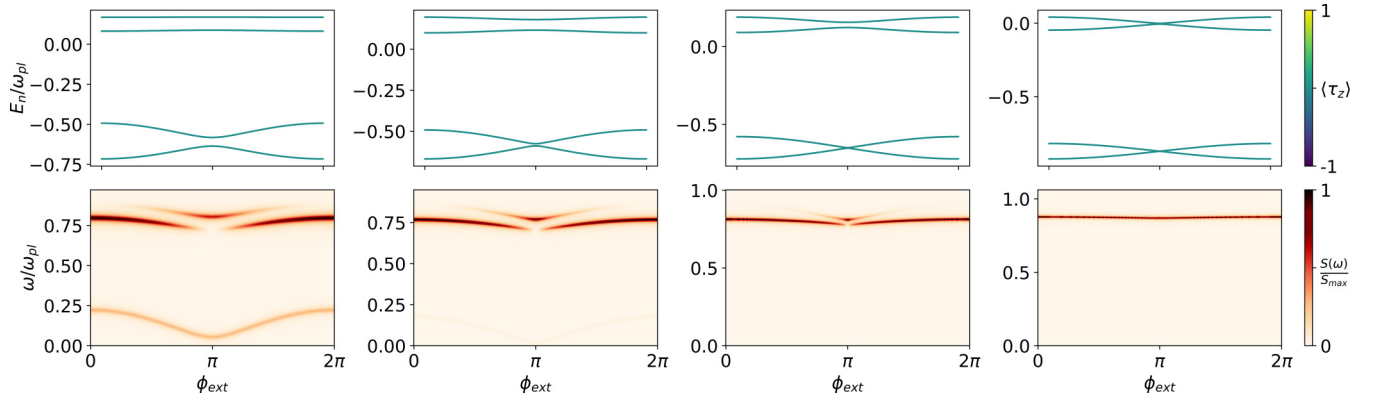


FIG. 10. Full evolution of the energy spectrum and its MW response as a function of ϕ_{ext} at the sweet spot for $E_J/E_C = 1.5, 3, 5, 10$ (from left to right).

Hamiltonian (E1) is

$$H = \begin{pmatrix} h(n_g) + V_J^{11} & V_J^{12} e^{-i\frac{\phi}{2}} \\ e^{i\frac{\phi}{2}} V_J^{21} & h(n_g + \frac{1}{2}) + e^{i\frac{\phi}{2}} V_J^{22} e^{-i\frac{\phi}{2}} \end{pmatrix}, \quad (\text{E7})$$

and hence the site elements h_j^ϕ and v_{jk}^ϕ change according to this transformation.

2. Charge space

In charge representation, the set of states $\{|n\rangle\}_{n=-\infty}^{\infty}$ form an orthonormal basis of such space. Here, the number of Cooper pair operators is defined as

$$\hat{n} = \sum_{n=-\infty}^{\infty} n |n\rangle \langle n|, \quad (\text{E8})$$

whereas the action of its conjugate operator ϕ on each one of those states is

$$e^{ik\phi} |n\rangle = |n+k\rangle. \quad (\text{E9})$$

Therefore, the Hamiltonian (E1) can be expressed as

$$H = \sum_{n=-\infty}^{\infty} (n - n_g)^2 |n\rangle \langle n| + V_J(\phi), \quad (\text{E10})$$

where the form of the Josephson potential is conditioned by its phase-dependent terms, the most usual of which are

$$\begin{aligned} \cos(k\phi) &= \frac{1}{2} \sum_{n=-\infty}^{\infty} (|n+k\rangle \langle n| + \text{H.c.}), \\ \sin(k\phi) &= \frac{-i}{2} \sum_{n=-\infty}^{\infty} (|n+k\rangle \langle n| - \text{H.c.}). \end{aligned} \quad (\text{E11})$$

Indeed, for more complex potentials, we can perform a Fourier transform that reduces it to a simple sum of these terms. This representation gives rise to an identical spectrum to that calculated in phase space. However, in this case we require a smaller (truncated) number of sites N of the tight-binding Hamiltonian matrix, so this method needs less computational power and time than the other one. Note that, in phase space, $\text{dim} = 2N$ since each site is a spinor with two possible parities, whereas in charge space we have a set of states $\{|n\rangle\}$ ($n = -N, -N + 1/2, \dots, 0, 1/2, \dots, N$), so that $\text{dim} = 2N + 1$.

Indeed, Fig. 11 shows the convergence of the first four states as a function of N , defined as the maximum number of sites that discretize the tight-binding space. This convergence is defined as the distance between the curves that

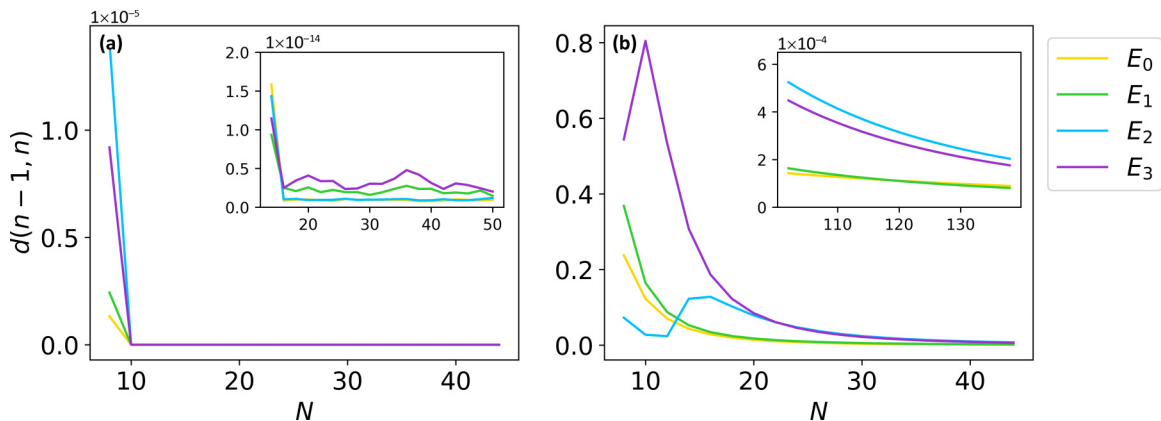


FIG. 11. Distance between curves $E_i^{N-1}(n_g)$ and $E_i^N(n_g)$ (where $i = 0, 1, 2, 3$ labels eigenstates of increasing energy) at the sweet spot as a function of a cutoff N . Numerical methods are implemented in (a) charge space and (b) phase space.

each eigenstate traces (as a function of n_g) with $N - 1$ and N sites. It is straightforward to see that the tight-binding

method converges much faster in charge space than in phase space.

-
- [1] M. Leijnse and K. Flensberg, Introduction to topological superconductivity and Majorana fermions, *Semicond. Sci. Technol.* **27**, 124003 (2012).
- [2] J. Alicea, New directions in the pursuit of Majorana fermions in solid state systems, *Rep. Prog. Phys.* **75**, 076501 (2012).
- [3] C. W. J. Beenakker, Search for Majorana fermions in superconductors, *Annu. Rev. Condens. Matter Phys.* **4**, 113 (2013).
- [4] R. Aguado, Majorana quasiparticles in condensed matter, *Riv. Nuovo Cimento* **40**, 523 (2017).
- [5] C. W. J. Beenakker, Search for non-Abelian Majorana braiding statistics in superconductors, *SciPost Phys. Lect. Notes* **15** (2020).
- [6] R. Aguado and L. P. Kouwenhoven, Majorana qubits for topological quantum computing, *Phys. Today* **73**, 44 (2020).
- [7] K. Flensberg, F. von Oppen, and A. Stern, Engineered platforms for topological superconductivity and Majorana zero modes, *Nat. Rev. Mater.* **6**, 944 (2021).
- [8] P. Marra, Majorana nanowires for topological quantum computation, *J. Appl. Phys.* **132**, 231101 (2022).
- [9] C. Nayak, S. H. Simon, A. Stern, M. Freedman, and S. Das Sarma, Non-abelian anyons and topological quantum computation, *Rev. Mod. Phys.* **80**, 1083 (2008).
- [10] E. Prada, P. San-Jose, M. W. A. de Moor, A. Geresdi, E. J. H. Lee, J. Klinovaja, D. Loss, J. Nygård, R. Aguado, and L. P. Kouwenhoven, From Andreev to Majorana bound states in hybrid superconductor–semiconductor nanowires, *Nat. Rev. Phys.* **2**, 575 (2020).
- [11] M. Leijnse and K. Flensberg, Parity qubits and poor man’s Majorana bound states in double quantum dots, *Phys. Rev. B* **86**, 134528 (2012).
- [12] J. D. Sau and S. D. Sarma, Realizing a robust practical Majorana chain in a quantum-dot-superconductor linear array, *Nat. Commun.* **3**, 964 (2012).
- [13] C.-X. Liu, G. Wang, T. Dvir, and M. Wimmer, Tunable superconducting coupling of quantum dots via Andreev bound states in semiconductor-superconductor nanowires, *Phys. Rev. Lett.* **129**, 267701 (2022).
- [14] A. Tsintzis, R. S. Souto, and M. Leijnse, Creating and detecting poor man’s Majorana bound states in interacting quantum dots, *Phys. Rev. B* **106**, L201404 (2022).
- [15] R. Seoane Souto, A. Tsintzis, M. Leijnse, and J. Danon, Probing Majorana localization in minimal Kitaev chains through a quantum dot, *Phys. Rev. Res.* **5**, 043182 (2023).
- [16] A. Bordin, G. Wang, C.-X. Liu, S. L. D. ten Haaf, N. van Loo, G. P. Mazur, D. Xu, D. van Driel, F. Zatelli, S. Gazibegovic, G. Badawy, E. P. A. M. Bakkers, M. Wimmer, L. P. Kouwenhoven, and T. Dvir, Tunable crossed Andreev reflection and elastic cotunneling in hybrid nanowires, *Phys. Rev. X* **13**, 031031 (2023).
- [17] Q. Wang, S. L. D. ten Haaf, I. Kulesh, D. Xiao, C. Thomas, M. J. Manfra, and S. Goswami, Triplet correlations in Cooper pair splitters realized in a two-dimensional electron gas, *Nat. Commun.* **14**, 4876 (2023).
- [18] A. Tsintzis, R. Seoane Souto, K. Flensberg, J. Danon, and M. Leijnse, Roadmap towards Majorana qubits and nonabelian physics in quantum dot-based minimal Kitaev chains, [arXiv:2306.16289](https://arxiv.org/abs/2306.16289).
- [19] P. Boross and A. Pályi, Braiding-based quantum control of a Majorana qubit built from quantum dots, [arXiv:2305.08464](https://arxiv.org/abs/2305.08464).
- [20] T. Dvir, G. Wang, N. van Loo, C.-X. Liu, G. P. Mazur, A. Bordin, S. L. D. ten Haaf, J.-Y. Wang, D. van Driel, F. Zatelli, X. Li, F. K. Malinowski, S. Gazibegovic, G. Badawy, E. P. A. M. Bakkers, M. Wimmer, and L. P. Kouwenhoven, Realization of a minimal Kitaev chain in coupled quantum dots, *Nature (London)* **614**, 445 (2023).
- [21] N. Sedlmayr and C. Bena, Visualizing Majorana bound states in one and two dimensions using the generalized Majorana polarization, *Phys. Rev. B* **92**, 115115 (2015).
- [22] N. Sedlmayr, J. M. Aguiar-Hualde, and C. Bena, Majorana bound states in open quasi-one-dimensional and two-dimensional systems with transverse Rashba coupling, *Phys. Rev. B* **93**, 155425 (2016).
- [23] S. V. Aksenov, A. O. Zlotnikov, and M. S. Shustin, Strong Coulomb interactions in the problem of Majorana modes in a wire of the nontrivial topological class BDI, *Phys. Rev. B* **101**, 125431 (2020).
- [24] For the sake of simplicity, we assume in what follows that t_α and Δ_α are parameters of the model, but we note in passing that both can be obtained from a microscopic description of the middle segments mediating the interdot couplings [13,14].
- [25] E. Ginossar and E. Grosfeld, Microwave transitions as a signature of coherent parity mixing effects in the Majorana-transmon qubit, *Nat. Commun.* **5**, 4772 (2014).
- [26] A. Keselman, C. Murthy, B. van Heck, and B. Bauer, Spectral response of Josephson junctions with low-energy quasiparticles, *SciPost Phys.* **7**, 050 (2019).
- [27] K. Yavilberg, E. Ginossar, and E. Grosfeld, Fermion parity measurement and control in Majorana circuit quantum electrodynamics, *Phys. Rev. B* **92**, 075143 (2015).
- [28] T. Li, W. A. Coish, M. Hell, K. Flensberg, and M. Leijnse, Four-Majorana qubit with charge readout: Dynamics and decoherence, *Phys. Rev. B* **98**, 205403 (2018).
- [29] J. Ávila, E. Prada, P. San-Jose, and R. Aguado, Superconducting islands with topological Josephson junctions based on semiconductor nanowires, *Phys. Rev. B* **102**, 094518 (2020).
- [30] J. Ávila, E. Prada, P. San-Jose, and R. Aguado, Majorana oscillations and parity crossings in semiconductor nanowire-based transmon qubits, *Phys. Rev. Res.* **2**, 033493 (2020).
- [31] T. B. Smith, M. C. Cassidy, D. J. Reilly, S. D. Bartlett, and A. L. Grimsmo, Dispersive readout of Majorana qubits, *PRX Quantum* **1**, 020313 (2020).
- [32] E. Lupo, E. Grosfeld, and E. Ginossar, Implementation of single-qubit gates via parametric modulation in the Majorana transmon, *PRX Quantum* **3**, 020340 (2022).
- [33] P. San-Jose, E. Prada, and R. Aguado, ac Josephson effect in finite-length nanowire junctions with Majorana modes, *Phys. Rev. Lett.* **108**, 257001 (2012).
- [34] D. I. Pikulin and Y. V. Nazarov, Phenomenology and dynamics of a Majorana Josephson junction, *Phys. Rev. B* **86**, 140504(R) (2012).

- [35] M. Trif, O. Dmytruk, H. Bouchiat, R. Aguado, and P. Simon, Dynamic current susceptibility as a probe of Majorana bound states in nanowire-based Josephson junctions, *Phys. Rev. B* **97**, 041415(R) (2018).
- [36] J. Cayao, A. M. Black-Schaffer, E. Prada, and R. Aguado, Andreev spectrum and supercurrents in nanowire-based SNS junctions containing Majorana bound states, *Beilstein J. Nanotechnol.* **9**, 1339 (2018).
- [37] Note that in a realistic experimental circuit one would need extra elements not included in the model, such as extra gate-tunable junctions to effectively ground either of the two superconducting islands, a capacitive coupling to a resonator to perform dispersive readout, drive lines for gate operations, etc.
- [38] In practice, we solve the model as a tight-binding chain in charge space. Specifically, we divide the phase interval $\phi \in [0, 2\pi)$ in N steps, constructing a $2N \times 2N$ Hamiltonian matrix in tight-binding form. Then, we can move to its dual space of charge states $\{|n\rangle, |n + 1/2\rangle\}_{n=-N}^N$ and rewrite the tight-binding Hamiltonian in this basis by applying a Fourier transformation of the quantum phase operators (see Appendix E).
- [39] For graphical purposes, we have convolved this quantity with a Cauchy-Lorentz distribution ($\gamma = 0.05$), which yields a finite-line broadening of the spectra.
- [40] J. A. Schreier, A. A. Houck, J. Koch, D. I. Schuster, B. R. Johnson, J. M. Chow, J. M. Gambetta, J. Majer, L. Frunzio, M. H. Devoret, S. M. Girvin, and R. J. Schoelkopf, Suppressing charge noise decoherence in superconducting charge qubits, *Phys. Rev. B* **77**, 180502(R) (2008).
- [41] A. Kringhøj, B. van Heck, T. W. Larsen, O. Erlandsson, D. Sabonis, P. Krogstrup, L. Casparis, K. D. Petersson, and C. M. Marcus, Suppressed charge dispersion via resonant tunneling in a single-channel transmon, *Phys. Rev. Lett.* **124**, 246803 (2020).
- [42] A. Bargerbos, W. Uilhoorn, C.-K. Yang, P. Krogstrup, L. P. Kouwenhoven, G. de Lange, B. van Heck, and A. Kou, Observation of vanishing charge dispersion of a nearly open superconducting island, *Phys. Rev. Lett.* **124**, 246802 (2020).
- [43] T. Vakhtel and B. van Heck, Quantum phase slips in a resonant Josephson junction, *Phys. Rev. B* **107**, 195405 (2023).
- [44] D. M. T. van Zanten, D. Sabonis, J. Suter, J. I. Väyrynen, T. Karzig, D. I. Pikulin, E. C. T. O'Farrell, D. Razmadze, K. D. Petersson, P. Krogstrup, and C. M. Marcus, Photon-assisted tunnelling of zero modes in a Majorana wire, *Nat. Phys.* **16**, 663 (2020).
- [45] G. de Lange, B. van Heck, A. Bruno, D. J. van Woerkom, A. Geresdi, S. R. Plissard, E. P. A. M. Bakkers, A. R. Akhmerov, and L. DiCarlo, Realization of microwave quantum circuits using hybrid superconducting-semiconducting nanowire Josephson elements, *Phys. Rev. Lett.* **115**, 127002 (2015).
- [46] T. W. Larsen, K. D. Petersson, F. Kuemmeth, T. S. Jespersen, P. Krogstrup, J. Nygård, and C. M. Marcus, Semiconductor-nanowire-based superconducting qubit, *Phys. Rev. Lett.* **115**, 127001 (2015).
- [47] D. Sabonis, O. Erlandsson, A. Kringhøj, B. van Heck, T. W. Larsen, I. Petkovic, P. Krogstrup, K. D. Petersson, and C. M. Marcus, Destructive little-parks effect in a full-shell nanowire-based transmon, *Phys. Rev. Lett.* **125**, 156804 (2020).
- [48] J. Huo, Z. Xia, Z. Li, S. Zhang, Y. Wang, D. Pan, Q. Liu, Y. Liu, Z. Wang, Y. Gao, J. Zhao, T. Li, J. Ying, R. Shang, and H. Zhang, Gate-mon qubit based on a thin InAs-Al hybrid nanowire, *Chin. Phys. Lett.* **40**, 047302 (2023).
- [49] M. Hays, V. Fatemi, D. Bouman, J. Cerrillo, S. Diamond, K. Serniak, T. Connolly, P. Krogstrup, J. Nygård, A. L. Yeyati, A. Geresdi, and M. H. Devoret, Coherent manipulation of an Andreev spin qubit, *Science* **373**, 430 (2021).
- [50] A. Bargerbos, M. Pita-Vidal, R. Žitko, J. Ávila, L. J. Splitthoff, L. Grünhaupt, J. J. Wesdorp, C. K. Andersen, Y. Liu, L. P. Kouwenhoven, R. Aguado, A. Kou, and B. van Heck, Singlet-doublet transitions of a quantum dot Josephson junction detected in a transmon circuit, *PRX Quantum* **3**, 030311 (2022).
- [51] A. Bargerbos, M. Pita-Vidal, R. Žitko, L. J. Splitthoff, L. Grünhaupt, J. J. Wesdorp, Y. Liu, L. P. Kouwenhoven, R. Aguado, C. K. Andersen, A. Kou, and B. van Heck, Spectroscopy of spin-split Andreev levels in a quantum dot with superconducting leads, *Phys. Rev. Lett.* **131**, 097001 (2023).
- [52] M. Pita-Vidal, A. Bargerbos, R. Žitko, L. J. Splitthoff, L. Grünhaupt, J. J. Wesdorp, Y. Liu, L. P. Kouwenhoven, R. Aguado, B. van Heck, A. Kou, and C. K. Andersen, Direct manipulation of a superconducting spin qubit strongly coupled to a transmon qubit, *Nat. Phys.* **19**, 1110 (2023).
- [53] M. Hinderling, S. C. ten Kate, D. Z. Haxell, M. Coraiola, S. Paredes, F. K. E. Cheah, R. Schott, W. Wegscheider, D. Sabonis, and F. Nichele, Flip-chip-based fast inductive parity readout of a planar superconducting island, [arXiv:2307.06718](https://arxiv.org/abs/2307.06718).
- [54] G. C. Ménard, F. K. Malinowski, D. Puglia, D. I. Pikulin, T. Karzig, B. Bauer, P. Krogstrup, and C. M. Marcus, Suppressing quasiparticle poisoning with a voltage-controlled filter, *Phys. Rev. B* **100**, 165307 (2019).
- [55] H. Q. Nguyen, D. Sabonis, D. Razmadze, E. T. Manilla, V. F. Maisi, D. M. T. van Zanten, E. C. T. O'Farrell, P. Krogstrup, F. Kuemmeth, J. P. Pekola, and C. M. Marcus, Electrostatic control of quasiparticle poisoning in a hybrid semiconductor-superconductor island, *Phys. Rev. B* **108**, L041302 (2023).
- [56] W. Uilhoorn, J. G. Kroll, A. Bargerbos, S. D. Nabi, C.-K. Yang, P. Krogstrup, L. P. Kouwenhoven, A. Kou, and G. de Lange, Quasiparticle trapping by orbital effect in a hybrid superconducting-semiconducting circuit, [arXiv:2105.11038](https://arxiv.org/abs/2105.11038).
- [57] B. H. Elfeky, W. M. Strickland, J. Lee, J. T. Farmer, S. Shanto, A. Zarassi, D. Langone, M. G. Vavilov, E. M. Levenson-Falk, and J. Shabani, Quasiparticle dynamics in epitaxial Al-InAs planar Josephson junctions, *PRX Quantum* **4**, 030339 (2023).
- [58] Two-tone spectroscopy measurements used to detect the MW transitions described here are typically integrated in timescales of the order of tens of milliseconds; see, e.g., [42].
- [59] R. Aguado, A perspective on semiconductor-based superconducting qubits, *Appl. Phys. Lett.* **117**, 240501 (2020).